Non-aqueous hybrid supercapacitors fabricated with mesoporous TiO$_2$ microspheres and activated carbon electrodes with superior performance

Yong Cai, Bote Zhao, Jie Wang, Zongping Shao*

State Key Laboratory of Materials-Oriented Chemical Engineering, College of Chemistry & Chemical Engineering, Nanjing University of Technology, No. 5 Xin Mofan Road, Nanjing 210009, PR China

HIGHLIGHTS

- TiO$_2$ microspheres are synthesized and calcined from 400 to 1000 °C.
- A novel hybrid supercapacitor is fabricated using AC and TiO$_2$ microspheres.
- High energy density and power density are obtained with organic electrolyte.
- 98% of initial capacitance is remained after 1000 cycles at 1.0 A g^{-1}.

ARTICLE INFO

ABSTRACT

Mesoporous TiO$_2$ microspheres, synthesized by a facile template-free solvothermal method and subsequent heat treatment, are exploited as the electrode for hybrid supercapacitors. The effects of the calcination temperature on the phase composition, particulate microstructure and morphology are characterized by XRD, Raman, FE-SEM and N$_2$ adsorption/desorption measurements. Hybrid supercapacitors utilizing the as-prepared TiO$_2$ mesoporous microspheres as the negative electrode and activated carbon (AC) as the positive electrode in a non-aqueous electrolyte are fabricated. The electrochemical performance of these hybrid supercapacitors is studied by galvanostatic charge–discharge and cyclic voltammetry (CV). The hybrid supercapacitor built from TiO$_2$ microspheres calcined at 400 °C shows the best performance, delivering an energy density of 79.3 Wh kg^{-1} at a power density of 178.1 W kg^{-1}. Even at a power density of 9.45 kW kg^{-1}, an energy density of 31.5 Wh kg^{-1} is reached. These values are much higher than the AC–AC symmetric supercapacitor. In addition, the hybrid supercapacitor exhibits excellent cycling performance, retaining 98% of the initial energy density after 1000 cycles. Such outstanding electrochemical performance of the hybrid supercapacitor is attributed to the matched reaction kinetics between the two electrodes with different energy storage mechanisms.

1. Introduction

Because of the increasing demand for high-quality energy supplies for mobile, portable and stationary applications, various types of electrochemical energy storage and conversion technologies, such as rechargeable batteries [1,2], supercapacitors [3,4], and fuel cells [5,6], have been developed and have received tremendous attention during the past decade because of increasing concerns about energy saving and environmental protection from the public. Secondary batteries, in particular lithium-ion batteries (LIBs), have widely served as power sources for personal electronics (laptop computers, cell phones, digital cameras, etc.). It is generally believed that such electrochemical devices also have great potential for other large-scale applications, such as power sources for electric and hybrid electric vehicles and energy storage for smart grids [7,8].

Different applications may have significantly different requirements for the scale of the energy and power supply. Modern sophisticated electronics and electric vehicles require power sources with high energy and power density, long cycling stability and outstanding safety. Traditional dielectric capacitors have very long cycle life, which can deliver high power in a very short time, while their energy density is pretty low. Rechargeable lithium-ion batteries show energy density as high as 200 Wh kg^{-1}, but they

---

* Corresponding author. Tel.: +86 25 83172256; fax: +86 25 83172242.
E-mail address: shaozp@njut.edu.cn (Z. Shao).

have a relatively low power density of <1 kW kg^{-1} and poor cycling stability with cycle life of typically <1000 cycles [9]. Recently, supercapacitors, also known as ultracapacitors or electrochemical capacitors have attracted attention. These devices store energy via electrochemical double layer capacitance (EDLC) or faradic pseudo capacitance and have an energy density (1–10 Wh kg^{-1}) much higher than conventional dielectric capacitor (<0.1 Wh kg^{-1}) and a power density (up to 10 kW kg^{-1}) higher than batteries (<1 kW kg^{-1}) [10–12]. To further narrow the energy/power gap between supercapacitors and lithium-ion batteries, a new type of electrochemical energy storage system, i.e., hybrid supercapacitor, was proposed. In this device, one electrode (typically the anode) uses secondary-battery-type lithium-intercalation materials while the other electrode (typically the cathode) contains electrochemical double layer capacitor-type carbon materials [13,14]. Such electrochemical devices store charges at the cathode through the reversible adsorption/desorption reaction of anions (PF_6^-, ClO_4^-, BF_4^-, etc.) and at the anode through a reversible lithium insertion/extraction reaction [15–17]. By taking advantage of this combination, hybrid supercapacitors have the potential to provide an energy density similar to LIBs as well as a high power density and long cycle life comparable with conventional EDLC supercapacitors [18].

During the past decades, several hybrid supercapacitors have been developed and studied, including carbon nanotubes (CNTs)–TiO$_2$ [19,20], activated carbon (AC)–TiO$_2$ [21], AC–Ni(OH)$_2$ [22], CNTs–Ni(OH)$_2$ [23], AC–RuO$_2$/TiO$_2$ nanotube composite [24], AC–Li$_4$Ti$_5$O$_{12}$ [25–27], AC–LiMn$_2$O$_4$ [28], AC–Li$_2$MnSiO$_4$ [29], AC–MnO$_2$ [30,31], AC–V$_2$O$_5$ [32], AC–Li$_2$FeSiO$_4$ [33], and AC–TiP$_2$O$_7$ [34]. These systems were comparable to secondary-battery-type electrode combinations with a carbon-type electrode; their maximum energy densities were generally less than 40 Wh kg^{-1} with most of them in the range of 10–20 Wh kg^{-1} or even lower. Because of the low cost, non-toxicity, environmental benignity and low solubility in organic electrolyte solution of TiO$_2$, the AC–TiO$_2$ hybrid supercapacitors are of particular interest [21,35–38]. However, due to the intrinsic difference in the energy storage mechanism between the AC and TiO$_2$ electrodes, the performance of the AC–TiO$_2$ supercapacitor is strongly limited by the mismatch of charge and discharge rates between the AC and TiO$_2$ electrodes [19]. The relatively low Li$^+$ diffusion coefficient and low electronic conductivity are the main obstacles to achieve high-power density in electrochemical devices with TiO$_2$ electrodes. Until now, the power and energy densities of AC–TiO$_2$ hybrid supercapacitors are still relatively low, and the energy density is usually lower than 42 Wh kg^{-1} [19–21]. TiO$_2$ has several polymorphs, including TiO$_2$(B), anatase, rutile and brookite [39]. Among them, the anatase and TiO$_2$(B) phases show the best electroactivity [35–38]. A morphological optimization can lead to further improvement in the electrode activity. For example, we demonstrated that mesoporous TiO$_2$(B)/anatase microspheres had excellent electrochemical performance in LIBs cycling within the potential range of 1.0–3.0 V [40].

In this work, we reported, for the first time, the adoption of mesoporous TiO$_2$ microspheres as anode materials for hybrid supercapacitors coupled with AC cathode in 1 M LiPF$_6$ (EC/DEC/DMC = 1:1:1) electrolyte cycling over a wide potential window of 0.0–2.8 V. The TiO$_2$ microspheres were prepared by a solvothermal process in combination with a subsequent thermal treatment. The effects of the calcination temperature on the morphology, structure and performance of TiO$_2$ in the hybrid supercapacitor were systematically studied. An energy density as high as 79.3 Wh kg^{-1} and excellent cycling stability were demonstrated for the hybrid supercapacitor. Such outstanding performance was discussed and explained.

2. Experimental

2.1. Powder synthesis

Hierarchical porous TiO$_2$ microspheres were synthesized by a solvothermal method [40]. Briefly, 1 mL of tetrabutyltitanate (TBT) (Shanghai Lingfeng Chemical Reagent Co., Ltd China) was added dropwise to a 50 mL acetic acid solution (Sinopharm Chemical Reagent Co., Ltd China) with vigorous stirring for 5 min and was then transferred into a Teflon-lined stainless-steel autoclave for solvothermal treatment at 150 °C for 24 h. The resulting precipitate was separated by centrifugation, washed with deionized water and ethanol, dried at 60 °C for 12 h to obtain white primary powder samples, and was then further calcined at 400, 500, 600, 700, 800, 900 or 1000 °C for 2 h in air to obtain the final products for later use.

2.2. Basic characterization

The structural properties of the synthesized TiO$_2$ powders were analyzed by X-ray powder diffraction (XRD) using a Bruker D8 advance diffractometer with filtered Cu Kα radiation ($\lambda \approx 0.154$ nm). The data were collected at room temperature with a scanning speed of 2° min^{-1} over a 2θ range of 10–80°. The Raman spectra were measured on a Horiba HR 800 with a 514-nm excitation line from an argon ion laser. The morphology and microstructure of the as-obtained products were examined using a field-emission scanning electron microscopy (FE-SEM, Hitachi S-4800). The N$_2$ adsorption–desorption measurement was carried out at the temperature of liquid nitrogen using a BELSORP II instrument. The specific surface area and pore size distribution of the samples were calculated using the Brunauer–Emmett–Teller (BET) method and the Barrett–Joyner–Halenda (BJH) method, respectively. Before analysis, the samples were pretreated at 200 °C for 2 h under vacuum.

2.3. Electrochemical characterization

The electrochemical performance test was performed using a typical two-electrode system [19]. The hybrid supercapacitors with TiO$_2$ microspheres as the active material of the negative electrode and commercial activated carbon (Nanjing XFnano Material Tech Co., Ltd China) as the active material of the positive electrode were fabricated as follows: First, 80 wt.% of the active material (TiO$_2$ or activated carbon), 10 wt.% of conductive Super P and 10 wt.% of PVDF (polyvinylidene fluoride) were mixed, and then they were directly added to an NMP (N-methyl pyrrolidinone) solution under continuous stirring for 10 h to make viscous slurries. Next, the as-prepared anode and cathode slurries were applied onto aluminum foils, which were pre-cleaned by sonicating in ethanol for 1 h. The electrode films were dried in a vacuum at 100 °C for 12 h, cut into disk shapes and finally assembled into hybrid supercapacitors in an Ar-filled glove-box. The weights of the disk-shaped films were typically 2 mg cm^{-2}. A non-aqueous solution composed of 1 M LiPF$_6$ dissolved in a mixture of ethylene carbonate (EC), diethyl carbonate (DEC), and dimethyl carbonate (DMC) with an EC/DEC/DMC volumetric ratio of 1:1:1 served as the liquid electrolyte. A microporous polypropylene film (Celgard 2400) was used as the separator. A lithium half-cell with TiO$_2$ as the working electrode and Li metal as the counter electrode was assembled using the same separator and electrolyte as the hybrid supercapacitors.

Charge–discharge curves of the two-electrode cells were recorded between 0.0 and 2.8 V at different current densities using a computer-controlled battery test station (Neware Battery Tester, Shenzhen, China). Cyclic voltammograms (CVs) were performed

over the potential range of 0.0–2.8 V at various sweep rates using a Princeton Applied Research PARSTAT 2273 (Advanced Measurement Technology Inc., USA) advanced electrochemical system. Electrochemical impedance spectroscopy (EIS) measurements were also carried out using a PARSTAT 2273 advanced electrochemical system over the frequency range of 100 kHz−0.01 Hz. All electrochemical measurements were carried out at room temperature.

3. Results and discussion

3.1. Phase composition

Fig. 1 shows the XRD patterns of the various samples after calcination of the solid precursors from the solvothermal synthesis in air at different temperatures between 400 and 1000 °C for 2 h. The XRD patterns of the sample calcined at 400 °C, labeled TiO_2 (400), can be indexed well based on a physical mixture of $TiO_2(B)$ and anatase TiO_2 (inset of Fig. 1). Raman spectra were also measured to obtain more information about the phase composition of the various samples. The characteristic Raman modes of anatase TiO_2 are typically located at 143, 196, 395, 515 and 639 cm^{-1}, while they appear at 119, 143, 196, 235, 515 and 639 cm^{-1} for $TiO_2(B)$ [41,42]. As shown in Fig. 2, the appearance of both Raman modes at 119, 235 and 395 cm^{-1} in the Raman spectra strongly supported the co-existence of anatase TiO_2 and $TiO_2(B)$ phases in the TiO_2 (400) sample. For the sample calcined at 500 °C, labeled TiO_2 (500), the diffraction peaks of $TiO_2(B)$ became very weak, and the main XRD patterns could be indexed to a single anatase phase, which suggests that the $TiO_2(B)$ in the sample was metastable and mostly converted into anatase TiO_2 at a calcination temperature of 500 °C. This conclusion was further supported by the disappearance of the characteristic peak in the Raman spectrum of $TiO_2(B)$ at 235 cm^{-1} (Fig. 2). With an increase in the calcination temperature up to 800 °C, the sample (TiO_2 (800)) maintained an anatase TiO_2 lattice structure, while the increased peak intensity suggested improved crystallinity. The successful survival of anatase TiO_2 was further supported by the corresponding Raman spectra shown in Fig. 2. As the temperature further increased to 900 °C, the intensity of the diffraction peaks related to the anatase TiO_2 phase in the corresponding XRD patterns decreased; however, some new diffraction peaks at 2θ of 27.5, 36.2, 41.3 and 56.7° appeared, which can be
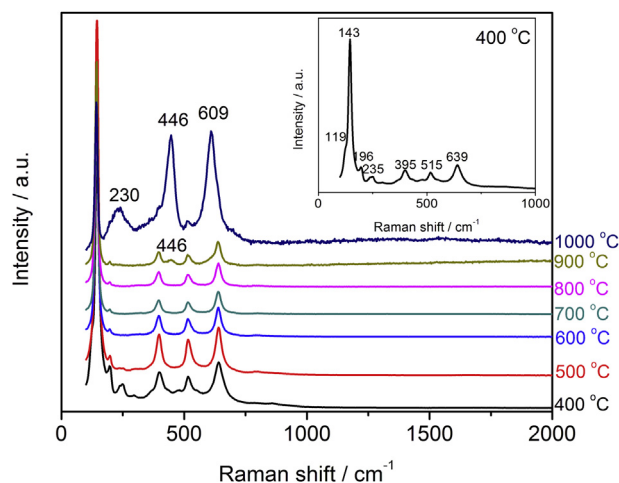

Fig. 2. Raman spectra of the TiO_2 calcined at various temperatures from 400 to 1000 °C; the inset is the Raman spectrum of TiO_2 calcined at 400 °C.

attributed to the (110), (101), (111) and (220) diffraction planes of rutile TiO_2 (JCPDS, No.: 65-0190), suggesting the partial conversion of anatase TiO_2 to rutile TiO_2. When the calcination temperature was further increased to 1000 °C, the peak intensity of the anatase phase reduced significantly, while the peak intensity of the rutile TiO_2 became much stronger, suggesting the anatase phase was largely converted to the rutile phase in TiO_2 (1000), supported by the significant change in the corresponding Raman spectrum. At a calcination temperature of 900 °C, a new peak at 446 cm^{-1} appeared in the Raman spectrum, while the peak at 639 cm^{-1} became broader on the low energy side, which suggests the presence of a shoulder peak at 609 cm^{-1}. Both peaks at 446 and 609 cm^{-1} are characteristic Raman modes for rutile TiO_2, implying the presence of rutile TiO_2 in the sample calcined at 900 °C. When the calcination temperature further increased to 1000 °C, a new peak at 230 cm^{-1} appeared for rutile TiO_2, and the intensity of the Raman modes for rutile TiO_2 became very strong, while the modes related to anatase TiO_2 were significantly reduced. Such results agree well with the XRD patterns. The exact phase compositions of the various samples were then determined by Rietveld refinement, and the results demonstrated that the samples calcined at 400, 500, 600, 700, 800, 900 and 1000 °C were composed of 81.9% anatase + 18.1% $TiO_2(B)$, 91.8% anatase TiO_2 + 8.2% $TiO_2(B)$, 100% anatase TiO_2, 100% anatase TiO_2, 100% anatase TiO_2, 85.3% anatase TiO_2 + 14.7% rutile TiO_2 and 22.4% anatase TiO_2 + 77.6% rutile TiO_2, respectively. Such a phase transition may have an effect on the electrode performance, which will be discussed in detail later.

3.2. Particulate morphology

Fig. 3 contains FE-SEM images of various samples calcined at different temperatures. The sample calcined at 400 °C, TiO_2 (400), was composed of microspheres with diameters of 2−4 μm, which were built by many nanosheets, as shown in the inset of Fig. 3a, similar to our previous observation for TiO_2 synthesized with the application of PVP [40]. Even after sintering at 700 °C, the microsphere morphological shape was still well maintained, and the diameter of the TiO_2 (700) spheres did not obviously change, which suggests that the phase transition from a mixture of anatase and $TiO_2(B)$ to anatase TiO_2 did not have any obvious effects on the particulate morphology. However, the nanosheets appeared to be somewhat sintered with an increase in the sintering temperature above 600 °C. As the calcination temperature further increased to
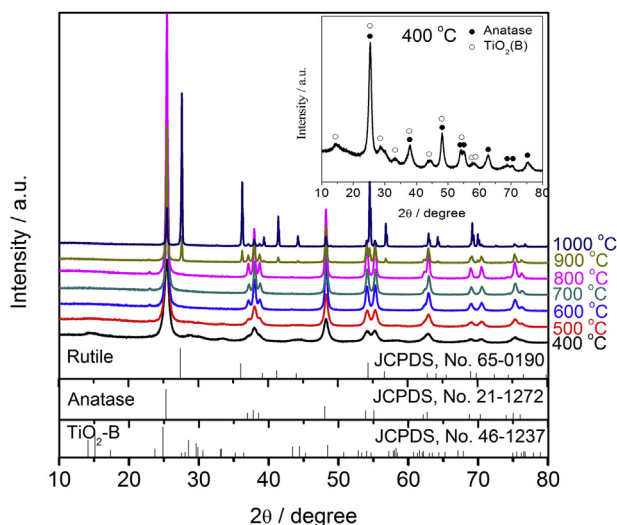

Fig. 1. XRD patterns of the TiO_2 calcined at various temperatures from 400 to 1000 °C; the inset is the XRD pattern of TiO_2 calcined at 400 °C.
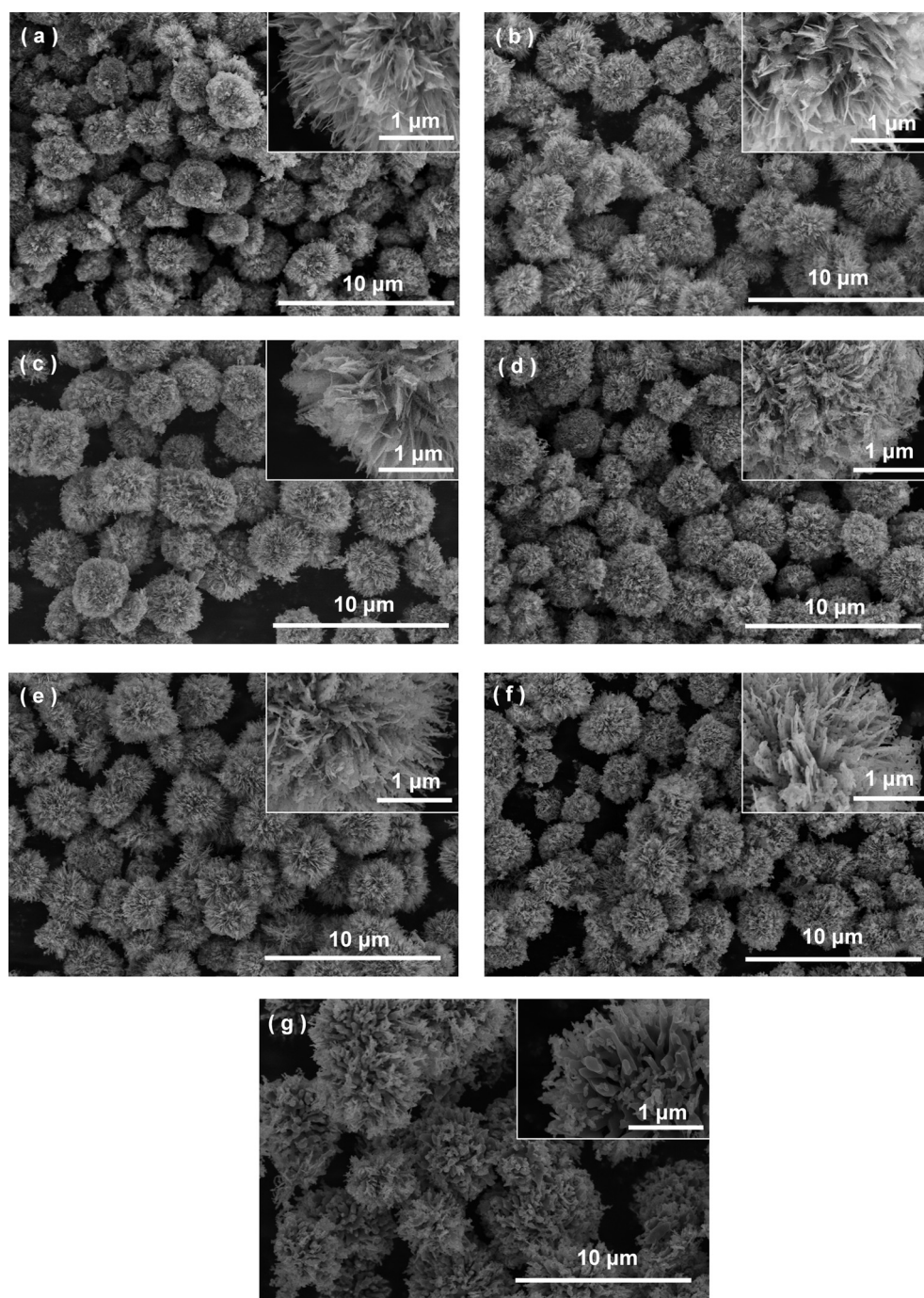
Fig. 3. FE-SEM images of the various TiO$_2$ calcined at different temperatures: (a) 400 °C, (b) 500 °C, (c) 600 °C, (d) 700 °C, (e) 800 °C, (f) 900 °C, and (g) 1000 °C; the insets are the magnified images.

800 °C, the nanosheets started to convert into nano bars, while the spherical structure of the secondary particles was still maintained even after the calcination at 1000 °C.

The pore structure of the samples calcined at different temperatures was examined using N$_2$ adsorption/desorption isotherms. Previously, we have demonstrated that the presence of PVP during the solvothermal synthesis caused the N$_2$ adsorption–desorption isotherm curve for the sample calcined at 400 °C to display a type IV isotherm with an H4 hysteresis loop in the range of 0.67–0.96 P/P_0, and the Barrett–Joyner–Halenda analysis showed the presence of two types of pores with pore sizes of ∼4.0 and

8.3 nm and a total pore volume of 0.5982 cm^3 g^{-1} [40]. Fig. 4 shows the typical N$_2$ adsorption–desorption isotherms and the related BJH pore size distribution curves of the samples calcined at the temperatures selected for this study (400, 500, 700 and 1000 °C). The pore sizes and pore volumes for the samples calcined at various temperatures are listed in Table 1. In this study, two types of pores were also observed for the samples calcined at 400 and 500 °C, but the relative volume of the two pores differed somewhat from the samples synthesized with PVP. Only one pore was observed for the samples calcined at 600–900 °C. The pores with sizes of approximately 4.0 nm were due to the arrangement of the TiO$_2$
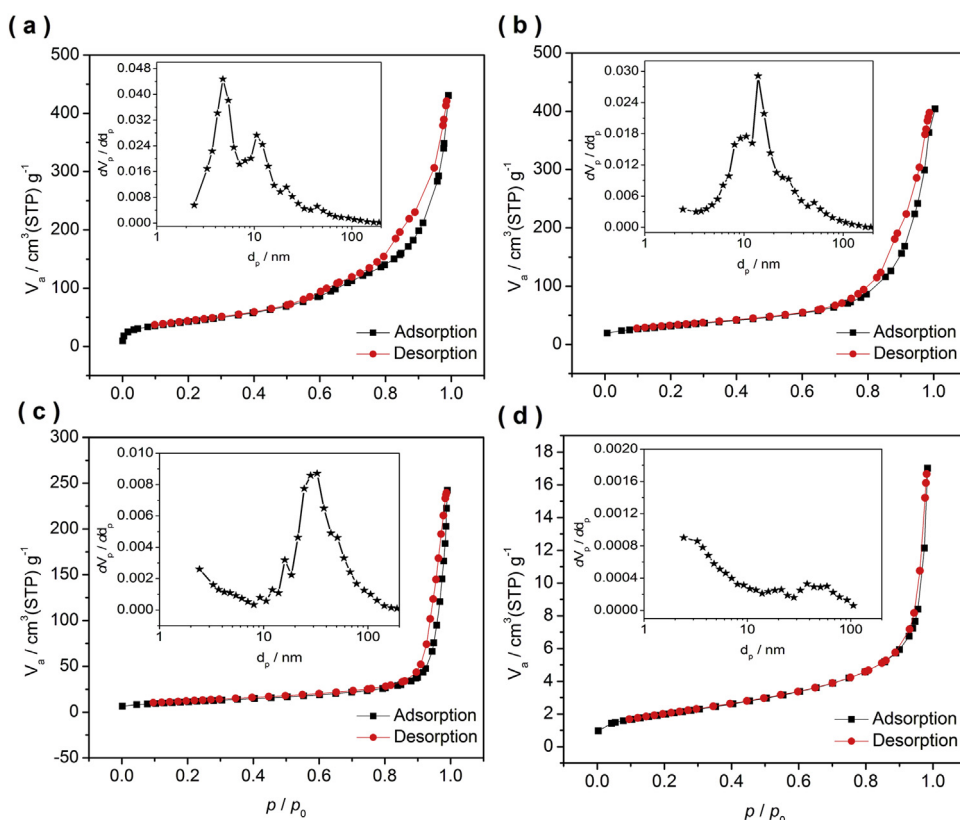
Fig. 4. N$_2$ adsorption/desorption curves of TiO$_2$ calcined at different temperatures: (a) 400 °C, (b) 500 °C, (c) 700 °C, and (d) 1000 °C; the insets are corresponding BJH pore distribution plots.

nanoparticles within the nanosheets, while the larger pores were due to the loose packing of those TiO$_2$ nanosheets [40], which suggests that the pores inside the nanosheets were almost eliminated at calcination temperatures above 600 °C due to the sintering of the particles. A monotonic decrease in the total pore volume due to thermal sintering was clearly demonstrated. Interestingly, the average pore diameter first increased with firing temperature, reached a maximum diameter of 36.6 nm at a calcination temperature of 700 °C, and then decreased with further increases in the firing temperature to only 14.8 nm for the sample calcined at 1000 °C. From the FE-SEM images, the nanosheets sintered into nano bars, and the microspheres shrank at calcination temperatures of 800 °C or higher, which may explain the corresponding decrease in pore size. The Brunauer–Emmett–Teller (BET) specific surface areas, calculated based on the nitrogen adsorption/desorption isotherms, were 157.1, 112.0, 82.2, 40.7, 29.9, 15.6 and 7.1 m^2 g^{-1} for the samples calcined at 400, 500, 600, 700, 800, 900 and 1000 °C, respectively. Clearly, an increase in the calcination temperature enhanced particulate sintering. At a calcination temperature of 1000 °C, the surface area was entirely from the outer surfaces of the particles because of the very small number of pores that survived.

3.3. Performance as lithium-intercalation electrode

To act as a Faradaic lithium-intercalation electrode in hybrid supercapacitors, the electrode should possess a high rate capability that matches the AC electrode, which realizes charge storage through a fast, non-Faradaic capacitative mechanism. Fig. 5a shows the typical galvanostatic discharge curves of electrodes calcined at different temperatures based on the half-cell configuration with a LiPF$_6$ electrolyte and metallic lithium counter and reference

electrodes over the potential range of 1.0–3.0 V at 0.2 A g^{-1} current density in 2nd cycle. For the electrodes calcined at 400 or 500 °C, two voltage platforms, one located at 1.75 V and the other at approximately 1.5–1.6 V were observed, suggesting the co-existence of both anatase TiO$_2$ (∼1.75 V) and TiO$_2$(B) (1.5–1.6 V) [41,42]. For the electrodes calcined at 600–800 °C, only one platform at approximately 1.75 V was observed, in agreement with a single anatase phase of the electrode material, as demonstrated by the XRD and Raman spectra shown in Figs. 1 and 2. For both the TiO$_2$ (900) and TiO$_2$ (1000) electrodes, a small shoulder at approximately 1.4 V was also observed in their galvanostatic discharge curves, which can be assigned to the intercalation of lithium into rutile TiO$_2$. The capacities in the second cycle are 203.3, 187.5, 160.5, 148.4, 140.5, 90.2 and 33.2 mAh g^{-1} for the electrodes calcined at 400, 500, 600, 700, 800, 900 and 1000 °C, respectively. The drop in capacity with calcination temperature over the range of 400–800 °C could be related to the sintering of the particles, and the transformation of anatase phase to rutile phase may contribute additional losses to the electrochemical activity due to the relative inertness of rutile TiO$_2$ to lithium intercalation [43]; these results suggest that the TiO$_2$ (400) sample is the most suitable electrode material for the lithium intercalation reaction, which may be related to its high specific surface area, hierarchical pore structure and rich TiO$_2$(B)/anatase TiO$_2$ phase boundaries. The discharge capacities of the electrode calcined at 400 °C at different current densities within the potential ranges of 1.0–3.0 V and 0.0–3.0 V are shown in Fig. 5b. The capacities in the potential range of 1.0–3.0 V were lower than the results from our previous studies mainly due to the absence of PVP in the solvothermal process [40]. It was interesting that at relatively low current densities, i.e., 0.25 and 0.5 A g^{-1}, higher capacities were demonstrated by discharging to 0.0 V than to 1.0 V; however, with a further increase in current

Table 1
BET specific surface area, average pore size and total pore volumes for the various TiO_2 samples calcined at different temperatures.

Temperature/°C	400	500	600	700	800	900	1000
Specific surface area/ $m^2\ g^{-1}$	157.12	112.02	82.24	40.72	29.88	15.62	7.13
Average pore diameter/nm	16.87	20.61	24.62	36.57	22.19	17.48	14.76
Total pore volume/ $cm^3\ g^{-1}$	0.654	0.577	0.506	0.372	0.166	0.068	0.026

density, the capacity decreased sharply to only 30.0 mAh g^{-1} at a current density of 3.0 A g^{-1}. For comparison, the sample retained 113.8 mAh g^{-1} by discharging over the potential range of 1.0–3.0 V, which suggests that excess Li^+ intercalation resulted in decreased reversibility for the lithium insertion/extraction. Furthermore, the solid-electrolyte interface (SEI) film on the active material surface and the additional electrolyte decomposition also increased the electrical resistance of the working electrode and reduced the rate capability [44,45]. We further investigated the cycling stability of TiO_2 (400) at a current density of 1.0 A g^{-1} over the potential ranges of 1.0–3.0 V and 0.0–3.0 V. As shown in Fig. 5c, after cycling 200 times between 1.0 and 3.0 V, a discharge capacity of 145 mAh g^{-1} was maintained, indicating a retention of 83.8% of the capacity for the first cycle. For cycling in the potential range of 0.0–3.0 V, an

initial capacity of 225 mAh g^{-1} was achieved, which decreased sharply over the first 20 cycles to only 111 mAh g^{-1} in the 25th cycle, and a capacity of only 57 mAh g^{-1} was retained after 200 discharge–charge cycles, which suggests that maintaining high stability by discharging TiO_2 to an end potential of 1.0 V is easy; however, significant improvement in the energy density could be achieved by expanding the potential range because the energy density is directly proportional to the square of the potential window. Thus, a larger potential window is preferred.

3.4. Electrochemical performance of hybrid supercapacitors

Hybrid supercapacitors were assembled by using the various as-prepared TiO_2 microspheres and commercial AC (specific surface area of 2650 $m^2\ g^{-1}$, average pore size of 2.14 nm and total pore volume of 1.42 $cm^2\ g^{-1}$) as the negative and positive electrode active materials, in equal weights, respectively. For comparison, an AC–AC symmetric supercapacitor was also assembled and tested. The device of the AC–TiO_2 hybrid supercapacitor was schematically illustrated in Fig. 6. For the AC electrode, the energy storage was based on an electrical double layer from a non-Faradaic process with the PF_6^- anion, whereas the energy storage for TiO_2 electrode was a Li^+ insertion process [21,25]. The possible charge/discharge process of the hybrid supercapacitor can be demonstrated as the following formulas:
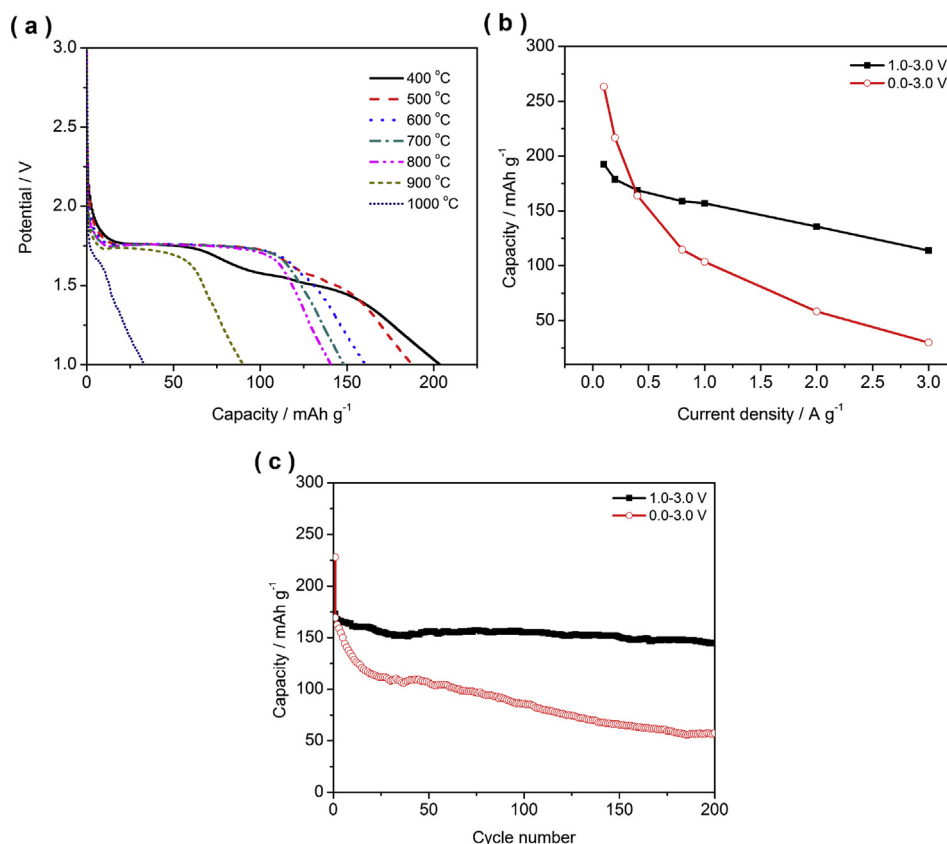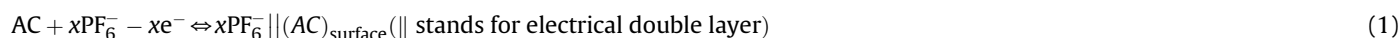
$$AC + xPF_6^- - xe^- \Leftrightarrow xPF_6^- \|(AC)_{surface} (\| \text{ stands for electrical double layer}) \tag{1}$$

Fig. 5. (a) The 2nd discharge curves of the TiO_2 calcined at different temperatures (0.2 A g^{-1}); (b) the 2nd discharge capacities of the TiO_2 calcined at 400 °C in the potential ranges of 1.0–3.0 V and 0.0–3.0 V at different current densities; (c) cycling performance of the TiO_2 calcined at 400 °C in the potential ranges of 1.0–3.0 V and 0.0–3.0 g^{-1} at 1.0 A g^{-1}.
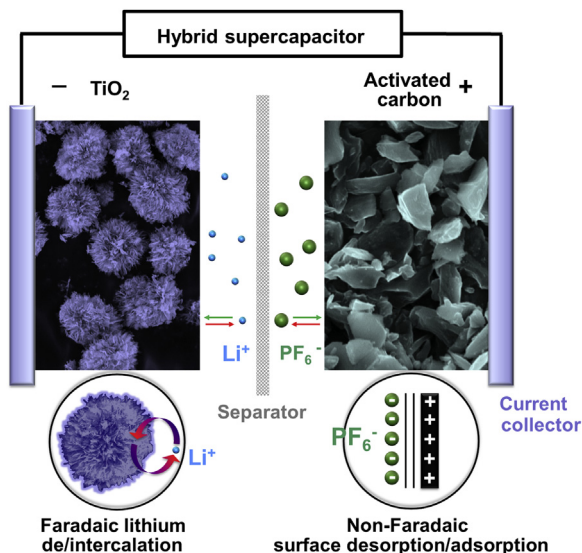
Fig. 6. Schematic illustration of AC–TiO$_2$ hybrid supercapacitor in non-aqueous electrolyte.

Fig. 7. (a) Galvanostatic charge/discharge curves at 0.2 A g^{-1} and (b) cyclic voltammograms at 20 mV s^{-1} of AC–TiO$_2$ hybrid supercapacitors and AC–AC symmetric supercapacitor.

$$x\mathrm{Li}^+ + \mathrm{TiO_2} + x\mathrm{e}^- \Leftrightarrow \mathrm{Li}_x\mathrm{TiO_2} \qquad (2)$$

The galvanostatic charge/discharge curves of the AC–AC symmetric supercapacitor and AC–TiO$_2$ hybrid supercapacitors at a current density of 0.2 A g^{-1} (with the respect to total mass of the active materials) are shown in Fig. 7a. For both types of the hybrid supercapacitors, except AC–TiO$_2$ (1000), an approximately linear response of the cell potential to time was demonstrated in their charge/discharge curves, suggesting good reversibility of the electrochemical charge/discharge process. The discharge curves of the AC–AC symmetric supercapacitor were highly symmetric with respect to their corresponding charge counterparts. This result is typical for charge–discharge curves of electric double layer supercapacitors and reflects energy storage via electrostatic surface-charge accumulation [10,19]. However, the shapes of the charge/discharge curves for the AC–TiO$_2$ hybrid supercapacitors exhibited a deviation from the curves of the AC–AC symmetric supercapacitor. In addition, the current–resistance (I–R) drop was relatively large and caused by the low electronic conductivity of the TiO$_2$ material [46–48]. All of the above differences between the AC–AC symmetric supercapacitor and the AC–TiO$_2$ hybrid supercapacitors revealed that the Faradaic reaction likely occurred in the TiO$_2$ microspheres. As a whole, a decrease in the discharge time with increasing calcination temperature was observed; in particular, the TiO$_2$ (900) and TiO$_2$ (1000) samples, in which TiO$_2$ had rutile structure, showed much shorter discharge times, suggesting decreased capacitance.

The electrochemical performance of both types of supercapacitors was further investigated using galvanostatic charge/discharge and CV measurements. Fig. 7b shows the steady-state cycle voltammograms within the potential window from 0.0 to 2.8 V at a rate of 20 mV s^{-1}. The curve from the AC–AC symmetric supercapacitor showed ideal rectangular shapes, indicating excellent capacitative behavior; however, all curves from the AC–TiO$_2$ hybrid supercapacitors deviated from the ideal rectangular shape. As the calcination temperature increased, the corresponding response current of the hybrid supercapacitor decreased, indicating a decrease in capacity with an increase in calcination temperature for the TiO$_2$ electrode. This result is consistent with the results of the galvanostatic charge/discharge experiments.
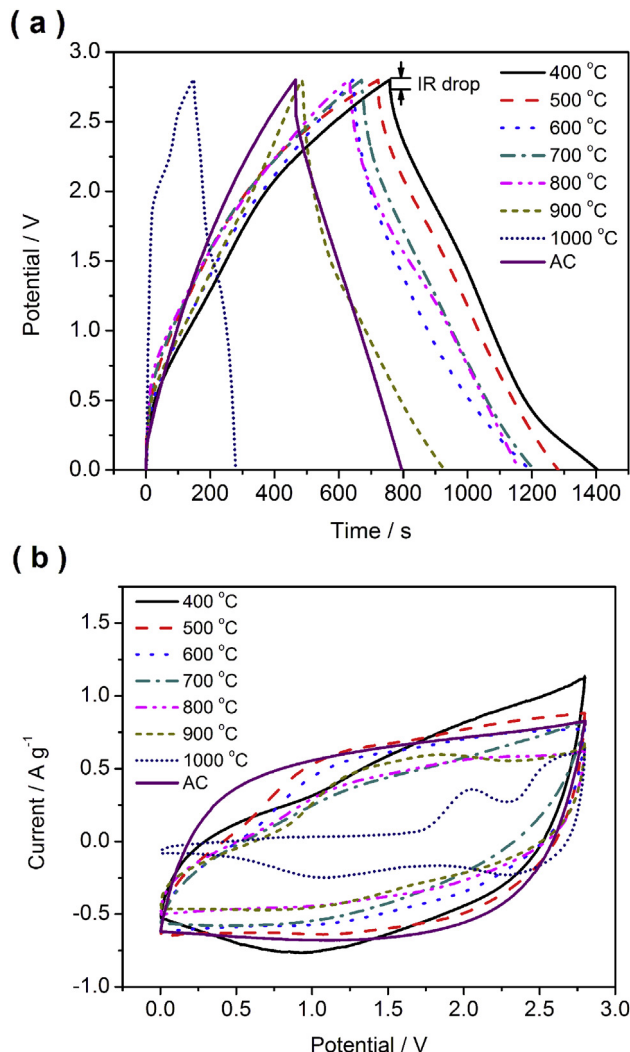
Based on the above analysis, TiO$_2$ (400) showed the best electrochemical performance as an electrode in hybrid supercapacitors. The CVs for the AC–AC symmetric supercapacitor and the AC–TiO$_2$ (400) hybrid supercapacitor at scan rates ranging from 5 to 50 mV s^{-1} were further investigated, and the results are shown in Fig. 8. According to the shapes of these curves, the current responses at the same voltage increased with the scan rate. The cycle voltammograms of the AC–AC symmetric supercapacitor maintained the ideal rectangular shapes, even at the fastest scan rate of 50 mV s^{-1}, indicating good electric double layer performance. As expected, the AC–TiO$_2$ hybrid supercapacitor gradually deviated from the ideal rectangular shape as the scan rate increased. As to the positive electrode, the highly reversible, non-Faradaic reaction occurred at the AC electrode/liquid electrolyte interface, where energy was stored by electrostatic surface-charge accumulation. By contrast, the energy stored in the TiO$_2$ negative electrode occurred by a lithium-intercalation reaction, where a Faradaic process along with reversible phase transformation and electron transfer occurred [19–21]. The overlapping effects of the pseudocapacitive contributions from the TiO$_2$ negative electrode and the double layer contribution from the AC positive electrode led to the deviation from ideal rectangular shape in the CV curves with increasing scan rate for the hybrid supercapacitor [19–21].
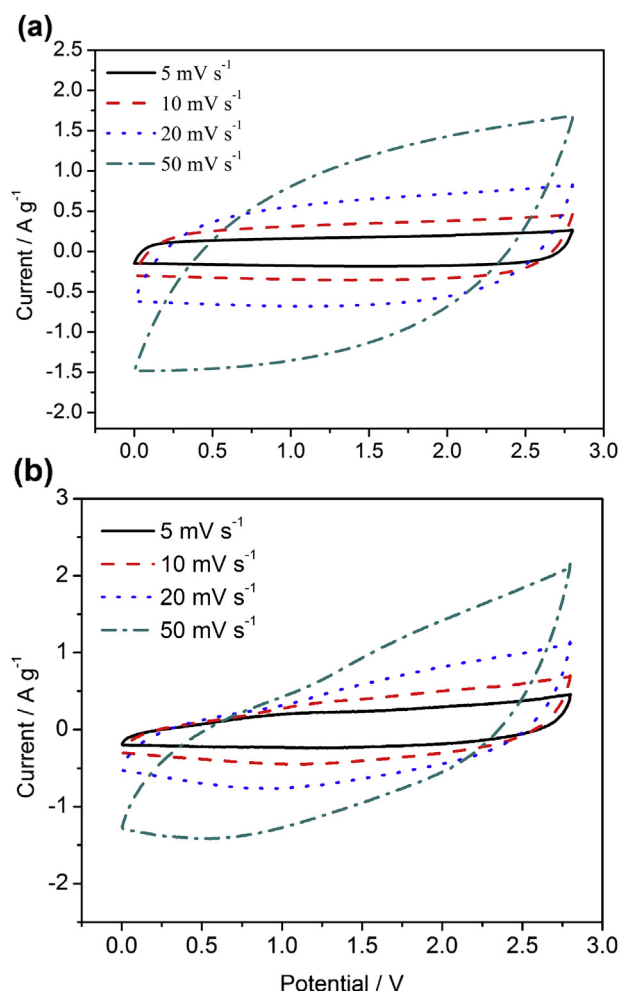
(a)

(b)

Fig. 8. Cyclic voltammograms of (a) AC–AC symmetric supercapacitor; (b) AC–TiO$_2$ (400) hybrid supercapacitor at various sweep rates.

(a)

(b)

Fig. 9. (a) Galvanostatic charge–discharge curves of AC–TiO$_2$ (400) hybrid supercapacitor at different current densities; (b) Ragone plots of power density versus energy density for AC–AC symmetric supercapacitor and AC–TiO$_2$ (400) hybrid supercapacitor.

To demonstrate the rate performance, the AC–TiO$_2$ (400) hybrid supercapacitor was further tested by galvanostatic charge–discharge over the potential range of 0.0–2.8 V at various current densities, and the results are shown in Fig. 9a. The specific capacitance of a hybrid supercapacitor (F g^{-1}) can be calculated according to the following equation:

$$C = \frac{I \times \Delta t}{M \times \Delta V} \qquad (3)$$

where M (g) is the total mass of the active materials in both electrodes, ΔV (V) is the operating potential window, I (A) is the constant discharge current and Δt (s) is the discharge time. Specific capacitances of 72.8, 59.6, 48.0, 40.1, 37.0, 29.5 and 28.9 F g^{-1} at current densities of 0.1, 0.2, 0.4, 0.8, 1.0, 2.0 and 3.0 A g^{-1}, respectively, were obtained for the AC–TiO$_2$ (400) hybrid supercapacitor. The specific capacitance maintained 40.0% of the capacitance at 0.1 A g^{-1} when the current density increased to 3.0 A g^{-1}, showing the outstanding rate performance of the hybrid supercapacitor. For the electrodes of supercapacitors, such as TiO$_2$, the energy is stored via a Faradaic reaction that occurs over the entire electrode surface or subsurface. Thus, a high specific surface is beneficial for achieving a high capacity. The unique hierarchical nano- and microstructures allowed for good penetration of the liquid electrolyte to the electrode surface, which allows for fast interfacial reactions.
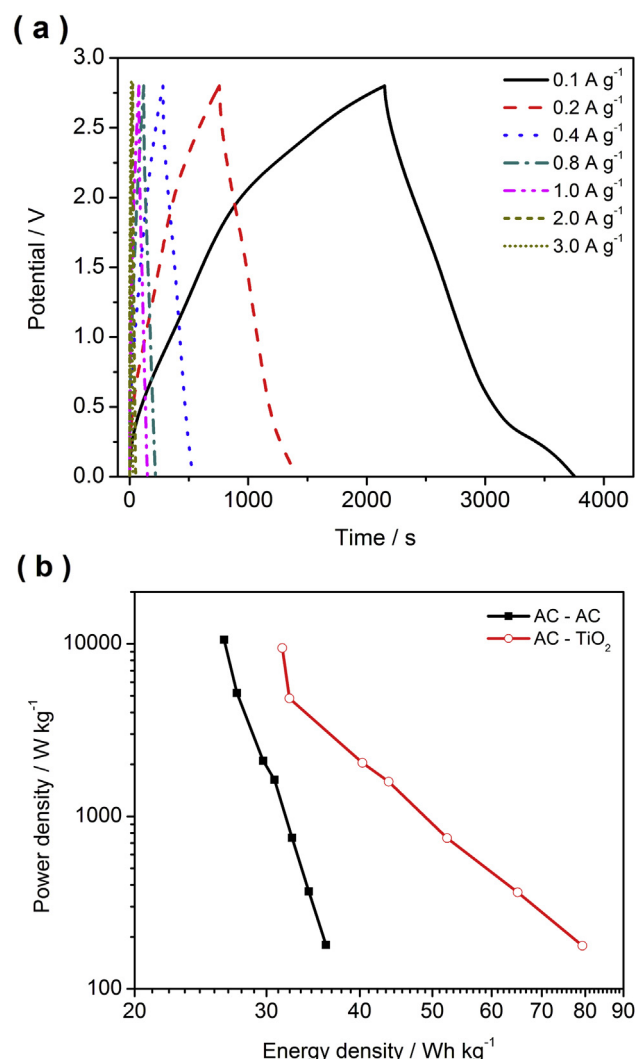
The mesoporous hierarchical structure also allows for good electron transport and efficient current collection. As a result, a high capacity and an excellent rate capacity were observed [49,50]. The energy density and power density are also important parameters for the electrochemical performance of supercapacitor. The energy density and power density of a supercapacitor can be calculated from the following equations:

$$E = 0.5C(\Delta V)^2 \qquad (4)$$

$$P = \frac{E}{\Delta t} \qquad (5)$$

where E (Wh kg^{-1}), C (F g^{-1}), ΔV (V), Δt (s) and P (W kg^{-1}) are the energy density, specific capacitance, the operating potential window, discharge time and power density, respectively. The power density will increase and the energy density will decrease with increasing current density. The Ragone plots of the AC–AC symmetric supercapacitor and the AC–TiO$_2$ (400) hybrid supercapacitor are presented in Fig. 9b to show the relationship between the energy density and the power density. The energy densities

were much higher in the AC–TiO$_2$ (400) hybrid supercapacitor than the AC–AC symmetric supercapacitor, especially at low power densities. The AC–TiO$_2$ (400) hybrid supercapacitor could obtain the highest energy density of 79.3 Wh kg^{-1} at a current density of 0.1 A g^{-1}; the energy density of the AC–AC symmetric supercapacitor (36.1 Wh kg^{-1}) was only 45.5% of the energy density of the AC–TiO$_2$ (400) hybrid supercapacitor, which is due to the previously mentioned advantages of the hybrid system. As for the AC–TiO$_2$ (400) hybrid supercapacitor, the energy density reached 79.3 Wh kg^{-1} at a power density of 178.1 W kg^{-1}, and the energy density was still 31.5 Wh kg^{-1} when the power density was increased to 9.45 kW kg^{-1}. The maximum energy density of the AC–TiO$_2$ (400) hybrid supercapacitor is much higher than the values reported for hybrid supercapacitors of CNTs–TiO$_2$(B) nanowires (12.5 Wh kg^{-1}) [19], CNTs–TiO$_2$ (B) nanotubes (19.3 Wh kg^{-1}) [20], or AC–TiO$_2$ anatase nanoparticles grown on the reduced graphene oxide (42 Wh kg^{-1}) [21]. It should be noted that the energy density (Wh kg^{-1}) and power density (W kg^{-1}) in our work are calculated based on the both mass of the electrode active materials (AC and TiO$_2$). The superior energy density of the hybrid supercapacitor can be attributed to its high specific capacitance and elevated cell voltage of 2.8 V in the non-aqueous electrolyte. In addition, the high energy densities delivered by the AC–TiO$_2$ (400) hybrid supercapacitor in our work have not been optimized, and the energy densities can be enhanced by the balancing of active masses of the two electrodes or changing the test condition in further work. Therefore, we believe that this hybrid supercapacitor may be considered a promising energy storage device that is suitable for various applications that require high energy density and high power density.

EIS of the cell were measured, and the corresponding Nyquist plots of AC–AC symmetric supercapacitor and AC–TiO$_2$ (400) hybrid supercapacitor over the frequency range from 100 kHz to 0.01 Hz are shown in Fig. 10a. The two impedance spectra appeared to be similar and consisted of a semicircle in the high-frequency region and a near-vertical line in the low-frequency region. The semicircle was related to the charge-transfer process while the linear region was caused by Warburg impedance. At high frequencies, the intercept with the real axis (Z$_{Re}$) can treated as the electrolyte resistance [51]. Obviously, the diameter of the semicircle for AC–AC was smaller than for AC–TiO$_2$ (400), suggesting low contact and charge-transfer impedances and good kinetic processes in the AC–AC symmetric supercapacitor. The low electronic conductivity of the TiO$_2$ microspheres and the different energy storage mechanisms of the AC and TiO$_2$ electrodes may account for some of the differences in the Nyquist plots of the AC–AC and AC–TiO$_2$ (400) supercapacitors [52]. From the Ragone plots, it is assumed that the overall kinetics of the AC–AC symmetric supercapacitor was an energy-limited process, whereas the AC–TiO$_2$ (400) hybrid supercapacitor was a power-limited process. Fig. 10b illustrates the Nyquist plots of the AC–TiO$_2$ (400) hybrid supercapacitor before and after 1000 cycles; there was no obvious change in the shape and size of the EIS after the cycling test. It could be speculated that the structure and composition of the electrodes have not changed after many cycles. The excellent cycling stability was further supported by repeated galvanostatic charge–discharge cycling tests. Fig. 11 shows the variation in energy density and coulombic efficiency as a function of cycle number for the AC–TiO$_2$ (400) hybrid supercapacitor at a current density of 1.0 A g^{-1} with a cell voltage of 0.0–2.8 V. The energy density showed a small decrease during the first 50 cycles. Then it increased gradually as the cycles continued and reached a stable value. After 1000 cycles, the energy density retained 98% of its initial value, and the coulombic efficiency remained stable above 95%, exhibiting excellent electrochemical stability. This result is consistent with our
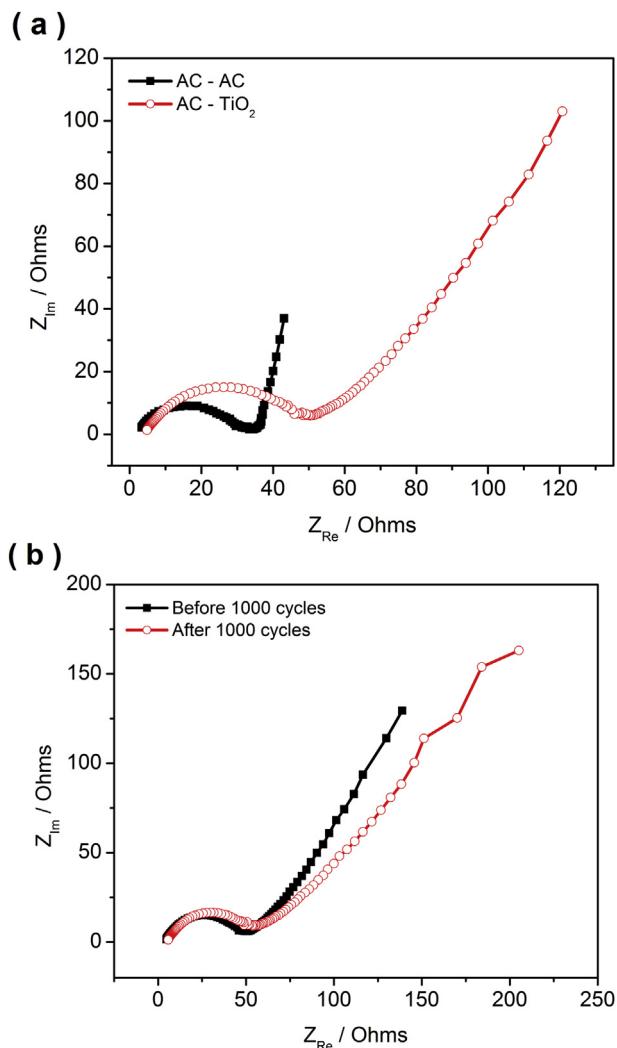

Fig. 10. EIS in Nyquist plots of: (a) AC–TiO$_2$ (400) hybrid supercapacitor and AC–AC symmetric supercapacitor before cycling; (b) AC–TiO$_2$ (400) hybrid supercapacitor before and after cycling.
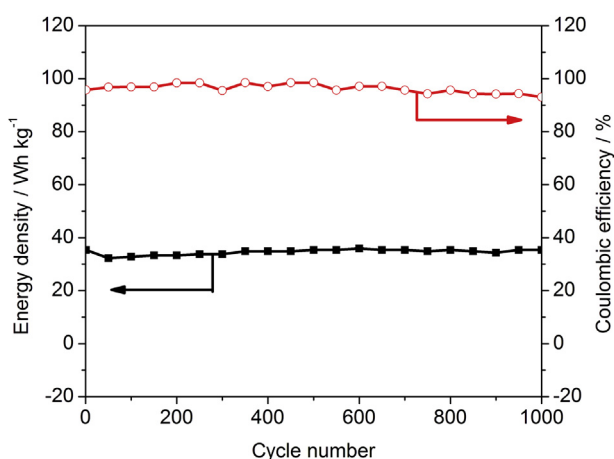

Fig. 11. Cycling stability in energy density and coulombic efficiency versus cycle number for AC–TiO$_2$ (400) hybrid supercapacitor.

previous results from the EIS. It is very interesting that TiO_2 was unstable when subjected to deep discharge to 0.0 V in lithium ion batteries. The favorable stability of the hybrid capacitor to cycling over the range of 0.0–2.8 V is likely due to the fact that in the hybrid supercapacitor, lithium insertion into TiO_2 only occurred at the surface; thus, the induced lattice strain was minimized.

4. Conclusions

In summary, mesoporous TiO_2 microspheres are synthesized by a facile template-free solvothermal method and subsequent heat treatment. And a novel hybrid supercapacitor, in which an AC positive electrode and TiO_2 negative electrode were well matched. The AC–TiO_2 (400) hybrid supercapacitor can deliver a maximum energy density of 79.3 Wh kg^{-1}, which is much higher than the AC–AC symmetry supercapacitor (36.1 Wh kg^{-1}). Additionally, this hybrid supercapacitor can achieve a very high power density (9.45 kW kg^{-1}) while maintaining an acceptable energy density (31.5 Wh kg^{-1}). The AC–TiO_2 (400) hybrid supercapacitor was quite stable during charge–discharge cycling and showed excellent cycling performance in this study. It can retain 98% capacitance of the initial after 1000 cycles. The AC–TiO_2 (400) hybrid supercapacitor exhibited excellent electrochemical performance in this study, which can be attributed to the synergistic effects of the different energy storage mechanisms in the two electrode materials. We believe that this hybrid supercapacitor deserves further investigation, as the results obtained in our work were not optimized. Therefore, the proposed AC–TiO_2 (400) hybrid supercapacitor may be considered a very promising energy storage device that is suitable for applications that require both high energy density and high power density.

Acknowledgments

References

[1] M.S. Whittingham, Chem. Rev. 104 (2004) 4271–4302.
[2] J. Hassoun, K. Lee, Y. Sun, B. Scrosati, J. Am. Chem. Soc. 133 (2011) 3139–3143.
[3] J.R. Miller, P. Simon, Science 321 (2008) 651–652.
[4] P. Simon, Y. Gogotsi, Nat Mater. 7 (2008) 845–854.
[5] Z. Shao, S.M. Haile, Nature 431 (2004) 170–173.
[6] Z. Shao, C. Zhang, W. Wang, C. Su, W. Zhou, Z. Zhu, H.J. Park, C. Kwak, Angew. Chem. Int. Ed. 123 (2011) 1832–1837.
[7] P. Thounthong, S. Raël, B. Davat, J. Power Sources 193 (2009) 376–385.
[8] M. Winter, R.J. Brodd, Chem. Rev. 104 (2004) 4245–4270.
[9] F. Zhang, T. Zhang, X. Yang, L. Zhang, K. Leng, Y. Huang, Y. Chen, Energy Environ. Sci. 6 (2013) 1623–1632.
[10] B.E. Conway, Electrochemical Supercapacitors: Scientific Fundamentals and Technological Applications, Plenum Publisher, New York, 1999.
[11] Y. He, W. Chen, X. Li, Z. Zhang, J. Fu, C. Zhao, E. Xie, ACS Nano 7 (2012) 174–182.
[12] A. Pandolfo, A. Hollenkamp, J. Power Sources 157 (2006) 11–27.
[13] W.G. Pell, B.E. Conway, J. Power Sources 136 (2004) 334–345.
[14] B.E. Conway, W. Pell, J. Solid State Electrochem. 7 (2003) 637–644.
[15] A. Laforgue, P. Simon, J.F. Fauvarque, M. Mastragostino, F. Soavi, J.F. Sarrau, P. Lailler, M. Conte, E. Rossi, S. Saguatti, J. Electrochem. Soc. 150 (2003) A645–A651.
[16] G.G. Amatucci, F. Badway, A. Du Pasquier, T. Zheng, J. Electrochem. Soc. 148 (2001) A930–A939.
[17] K. Naoi, S. Ishimoto, Y. Isobe, S. Aoyagi, J. Power Sources 195 (2010) 6250–6254.
[18] C. Zhou, Y. Zhang, Y. Li, J. Liu, Nano Lett. 13 (2013) 2078–2085.
[19] Q. Wang, Z. Wen, J. Li, Adv. Funct. Mater. 16 (2006) 2141–2146.
[20] G. Wang, Z.Y. Liu, J.N. Wu, Q. Lu, Mater. Lett. 71 (2012) 120–122.
[21] H. Kim, M.Y. Cho, M.H. Kim, K.Y. Park, H. Gwon, Y. Lee, K.C. Roh, K. Kang, Adv. Eng. Mater. (2013), http://dx.doi.org/10.1002/aenm.201300467.
[22] Y. Wang, D. Zhou, D. Zhao, M. Hou, C. Wang, Y. Xia, J. Electrochem. Soc. 160 (2013) A98–A104.
[23] Z. Tang, Ch. Tang, H. Gong, Adv. Funct. Mater. 22 (2012) 1272–1278.
[24] Y. Wang, Z. Wang, Y. Xia, Electrochim. Acta 50 (2005) 5641–5646.
[25] H. Jung, N. Venugopal, B. Scrosati, Y. Sun, J. Power Sources 221 (2013) 266–271.
[26] L. Cheng, H. Liu, J. Zhang, H. Xiong, Y. Xia, J. Electrochem. Soc. 153 (2006) A1472–A1477.
[27] B.G. Lee, J.R. Yoon, J. Electr. Eng. Technol. 7 (2012) 207–211.
[28] Y. Wang, Y. Xia, Electrochem. Commun. 7 (2005) 1138–1142.
[29] K. Karthikeyan, V. Aravindan, S. Lee, I. Jang, H. Lim, G. Park, M. Yoshio, Y. Lee, J. Power Sources 195 (2010) 3761–3764.
[30] L. Demarconnay, E. Raymundo-Piñero, F. Béguin, J. Power Sources 196 (2011) 580–586.
[31] P. Gao, A. Lu, W. Li, J. Power Sources 196 (2011) 4095–4101.
[32] L. Chen, Q. Lai, Y. Hao, Y. Zhao, X. Ji, J. Alloys Compd. 467 (2009) 465–471.
[33] K. Karthikeyan, V. Aravindan, S. Lee, I. Jang, H. Lim, G. Park, M. Yoshio, Y. Lee, J. Alloys Compd. 504 (2010) 224–227.
[34] V. Aravindan, M.V. Reddy, S. Madhavi, S.G. Mhaisalkar, G.V. Subba Rao, B.V.R. Chowdari, J. Power Sources 196 (2011) 8850–8854.
[35] T. Brousse, R. Marchand, P.-L. Taberna, P. Simon, J. Power Sources 158 (2006) 571–577.
[36] H. Liu, Z. Bi, X.G. Sun, R.R. Unocic, M.P. Paranthaman, S. Dai, G.M. Brown, Adv. Mater. 23 (2011) 3450–3454.
[37] P. Kubiak, J. Geserick, N. Hüsing, M. Wohlfahrt-Mehrens, J. Power Sources 175 (2008) 510–516.
[38] A.G. Dylla, J.A. Lee, K.J. Stevenson, Langmuir 28 (2012) 2897–2903.
[39] B. Zhao, S. Jiang, C. Su, R. Cai, R. Ran, M.O. Tadé, Z. Shao, J. Mater. Chem. A 1 (2013) 12310–12320.
[40] J. Wang, Y. Zhou, Z. Shao, Electrochim. Acta 97 (2013) 386–392.
[41] T. Beuvier, M. Richard-Plouet, L. Brohan, J. Phys. Chem. C 113 (2009) 13703–13706.
[42] T. Beuvier, M. Richard-Plouet, M. Mancini-Le Granvalet, T. Brousse, O. Crosnier, L. Brohan, Inorg. Chem. 49 (2010) 8457–8464.
[43] Y.S. Hu, L. Kienle, Y.G. Guo, J. Maier, Adv. Mater 18 (2006) 1421–1426.
[44] A. Phuruangrat, J.S. Chen, X.W. Lou, O. Yayapao, S. Thongtem, T. Thongtem, Appl. Phys. A 107 (2012) 249–254.
[45] M.S. Park, G.X. Wang, Y.M. Kang, D. Wexler, S.X. Dou, H.K. Liu, Angew. Chem. Int. Ed. 119 (2007) 764–767.
[46] J. Wang, Y. Zhou, B. Xiong, Y. Zhao, X. Huang, Z. Shao, Electrochim. Acta 88 (2013) 847–857.
[47] D. Wang, D. Choi, J. Li, Z. Yang, Z. Nie, R. Kou, D. Hu, C. Wang, L.V. Saraf, J. Zhang, ACS Nano 3 (2009) 907–914.
[48] X. Xin, X. Zhou, J. Wu, X. Yao, Z. Liu, ACS Nano 6 (2012) 11035–11043.
[49] B. Liu, A. Khare, E.S. Aydil, ACS. Appl. Mater. Interfaces 3 (2011) 4444–4450.
[50] J. Jamnik, J. Maier, Phys. Chem. Chem. Phys. 5 (2003) 5215–5220.
[51] X. Du, C. Wang, M. Chen, Y. Jiao, J. Wang, J. Phys. Chem. C 113 (2009) 2643–2646.
[52] P. Bueno, E. Leite, J. Wang, J. Phys. Chem. B 107 (2003) 8868–8877.